

## Granular element method for three-dimensional discrete element calculations

Keng-Wit Lim and José E. Andrade<sup>\*,†</sup>

*Division of Engineering & Applied Science, California Institute of Technology, Pasadena, CA 91125, U.S.A.*

### SUMMARY

This paper endows the recently-proposed granular element method (GEM) with the ability to perform 3D discrete element calculations. By using non-uniform rational B-Splines to accurately represent complex grain geometries, we proposed an alternative approach to clustering-based and polyhedra-based discrete element methods whereby the need for complicated and ad hoc approaches to construct 3D grain geometries is entirely bypassed. We demonstrate the ability of GEM in capturing arbitrary-shaped 3D grains with great ease, flexibility, and without excessive geometric information. Furthermore, the applicability of GEM is enhanced by its tight integration with existing non-uniform rational B-Splines modeling tools and ability to provide a seamless transition from binary images of real grain shapes (e.g., from 3D X-ray CT) to modeling and discrete mechanics computations. Copyright © 2013 John Wiley & Sons, Ltd.

Received 2 November 2012; Revised 29 April 2013; Accepted 30 April 2013

**KEY WORDS:** granular element method; discrete element method; discrete mechanics; NURBS; multi-scale analysis

### 1. INTRODUCTION

In this paper, we describe a new formulation that enables the granular element method (GEM) to perform fully 3D calculations within the context of discrete element methods (DEMs). This development is motivated by our earlier work in GEM in two dimensions [1]. Corresponding with the extension from two to three dimensions, non-trivial algorithmic developments in GEM, to be described in this paper, are required. Here, we show that non-uniform rational Basis-Splines (NURBS) provide a natural and straightforward way of representing 3D arbitrary-shaped grains. With 3D GEM, we incorporate the advantages of free-form computer-aided graphics design technology in the simulation of real granular materials. Specifically, through NURBS, GEM is able to directly address two of the three key aspects of morphology, namely sphericity and roundness. The third aspect, surface roughness, is accounted for via effective interparticle friction coefficient, as it is usually performed in regular discrete element calculations. With the advantage of flexible and accurate shape representation, GEM could also serve as a bridge from binary images (e.g., from X-ray tomography) of grains to discrete mechanics analysis, providing the key for the computation of parameters that characterize the response of granular materials at the micromechanical level and that can be incorporated into multiscale frameworks, see for example [2]. Here, we present our development of GEM for convex grains; the contributions in this paper, however, are regarded as the necessary steps towards constructing a thorough 3D NURBS-based discrete element strategy. Accurate morphology is deemed one of the keys in the development of predictive discrete element calculations.

<sup>\*</sup>Correspondence to: José E. Andrade, Division of Engineering & Applied Science, California Institute of Technology, Pasadena, CA 91125, U.S.A.

<sup>†</sup>E-mail: jandrade@caltech.edu

The connection of particle morphology with macroscopic properties of geomaterials, for example, permeability and strength, is well established [3, 4]. For example, it has been shown in [3] that in the case of macroscopic strength of coarse-grained soils, particle morphology characterized by sphericity, roundness, and surface roughness all affect the mobilized strength in granular materials. This macroscopic effect is due to micromechanical features such as increased rotational frustration in angular packings under large shear deformations. In addition, critical state parameters, which have become central for constitutive modeling based on inelasticity, are shown to be intimately connected with particle morphology. Therefore, the ability of micromechanical models for granular materials to accurately capture particle morphology is of paramount importance if they are to correctly predict the macroscopic strength in real granular materials such as sands. These developments are still to emerge.

Existing DEM approaches account for particle morphology (shape) mostly via clustering [4, 5] and polyhedra [6–9]. Alternatives include spheropolygons [10], potential particles [11, 12], and superquadrics. The first two alternatives essentially use a simplex or polygon as a base geometry, which is then smoothed at the corners and edges. Superquadrics are defined through an implicit function controlling the ‘blockiness’ of the particles and are supersets of ellipses and ellipsoids [13]. DEM based on ellipses and ellipsoids [14, 15] appears to be the most popular approach after clustering and polyhedra. Although current DEM approaches have improved the shape representation capabilities of DEM over disks and spheres [16], computational results today remain mostly qualitative. This lack of predictive capability stems from DEM’s current inability to capture real particle morphology. Existing DEM approaches are still limited in terms of shape representation because their underlying formulations are based primarily on primitive geometries such as spheres and planes and/or simple analytical functions.

We focus our attention mostly on clustering and polyhedra DEM, but the arguments given here apply generally to the other alternatives as well. In principle, polyhedra-based discrete elements can be refined as much as needed for an arbitrarily accurate grain shape representation. In practice, however, this resolution increase makes the computational cost associated with narrow-phase contact detection and force calculations prohibitively expensive, especially in large-scale simulations. As such, polyhedra-based discrete elements tend to appear ‘blocky’, and their shape representation capabilities are not fully realized. The use of spheres in clustering or clumping techniques, although relatively less expensive, is unappealing because of the lack of continuity in the curvatures and tangents. For example, the grains appear ‘clumpy’ at locations where spheres overlap or clump, and the curvature at any point on a sphere is always positive. The geometrical anomalies associated with the clustering technique prevents it from enabling higher fidelity contact mechanics calculations without further numerical treatment. In this paper, we seamlessly bypass all of the aforementioned issues related to particle morphology by enabling the representation of complex particle boundaries using NURBS. This parametric representation allows us to accurately represent particle shape down to features encapsulated at scales much below the particle diameter. Also, local curvature is available using NURBS and can be readily utilized in contact force calculations. Hence, the new discrete element representation furnished by GEM, represents a radically different approach to granular mechanics calculations and brings the method one step closer to quantitative analysis.

The structure of the paper is as follows. In the first section, we review some basic theory of NURBS surfaces, which are used for representing grain shapes. Second, we present a description on the contact force calculation relevant to 3D GEM. Third, we summarize the basic equations of motion and the discrete update equations of GEM. We then present a numerical example to demonstrate the capability of GEM. We conclude this paper by discussing potential areas for improving GEM. Throughout this paper, we highlight key differences between 2D and 3D GEM where appropriate.

#### *Remark 1*

Although GEM uses the framework of classical DEM, it is distinct from classical DEM by the use of a completely different geometrical basis for shape representation. Some features that are unique to GEM include shape flexibility through NURBS and the availability of local curvature information. The NURBS basis can also serve as a platform for integration with isogeometric analysis methodologies [17].

*Remark 2*

An exact sphere representation is possible only by using a single NURBS patch. Alternatively, a ‘volley-ball’ six-patch sphere approximation can be used. Our target application for GEM is on modeling real grains, which are never perfectly spherical.

## 2. GRAIN GEOMETRY REPRESENTATION USING NURBS

To improve the predictive capability of discrete mechanics simulations, an accurate geometry representation of grain morphology (shape) with the ability to provide additional information such as local curvatures for contact calculations is required. In particular, the choice of geometry representation needs to strike a balance between complexity (i.e., spatial resolution) and computational cost. Free-form modeling technologies from computer-aided graphics design, namely NURBS, appear to have the potential to provide this required balance. Here, we proceed directly to the description of NURBS surfaces, building upon the information provided by the authors in our 2D GEM formulation [1]. NURBS are ubiquitous in the world of computer graphics and computer-aided design/computer-aided manufacturing (CAD/CAM) systems. They provide flexibility in representing arbitrary and complex geometries with much less information than conventional faceted or polygonal counterparts. Although the theory of NURBS as a whole is large, we will only focus on parts of the theory that are sufficient for an implementation of GEM. Further details on NURBS can be found in [18].

Important mathematical properties of NURBS for the grain shape representation and discrete mechanics calculations have already been mentioned in [1], and these properties continue to apply in the 3D setting. In what follows, we operate under the following two assumptions:

1. Each grain is topologically equivalent to a sphere, and hence can be ‘morphed’ from a NURBS sphere via an optimization or interpolation procedure.
2. Point contact between grains is assumed.

The aforementioned two assumptions are consistent with the representation of coarse-grained dry granular materials, for example, sand grains, which we typically model in geomechanics by using DEM. Furthermore, these assumptions allow us to take advantage of several existing NURBS manipulation algorithms (see for example [18, 19]) for shape generation and local contact detection calculations. For example, one can morph a sphere into shapes that conform to angular geometries.

Referring to Figure 1, we describe the grain geometry as what is called in the graphics community a ‘NURBS tensor product surface’  $\mathbf{P}(s, t)$ :

$$\mathbf{P}(s, t) = \sum_{i=0}^m \sum_{j=0}^n \left( \frac{w_{ij} N_{i,p}(s) N_{j,p}(t)}{\sum_{g=0}^m \sum_{h=0}^n w_{gh} N_{g,p}(s) N_{h,p}(t)} \right) \mathbf{P}_{ij} \quad (1)$$

where  $\mathbf{P}_{ij}$  are the control points,  $w_{ij}$  are the weights, and  $N_{i,p}(s)$  and  $N_{j,p}(t)$  are the B-Splines univariate basis functions of degree  $p$ , which define the tensor product. In this paper, we adhere to the convention in the computational geometry literature where the degree  $p = 0, 1, 2, 3$ , etc. refers to constant, linear, quadratic, cubic, etc., piecewise polynomials, respectively. For most cases, grain surfaces are adequately described as a bicubic patch  $p = 3$ . The control points define a control grid or mesh, analogous to the control polygon for the curve case [1]. As usual, the grain is enclosed in the convex hull of the control points. Hence, to define a NURBS surface, we must specify a knot vector for the  $S$  basis functions, and a second knot vector for the  $T$  basis functions. These two knot vectors partition the parametric  $(s, t)$  space into a grid as shown in Figure 1, analogous to parametric segments in the curve case. The operations on NURBS curves such as knot insertion and so on, as described in [1], extend directly to NURBS surfaces; we simply operate on each of the control curves. Thus, to insert a knot into the  $S$  knot vector for a NURBS surface, we insert the knot into each  $S$ -control curve of the NURBS surface. For simplicity, we use knot vectors that are clamped (or non-periodic) with  $l + p + 1$  knot values where  $l$  is the number of control points in each parametric direction ( $m + 1$  or  $n + 1$ ).

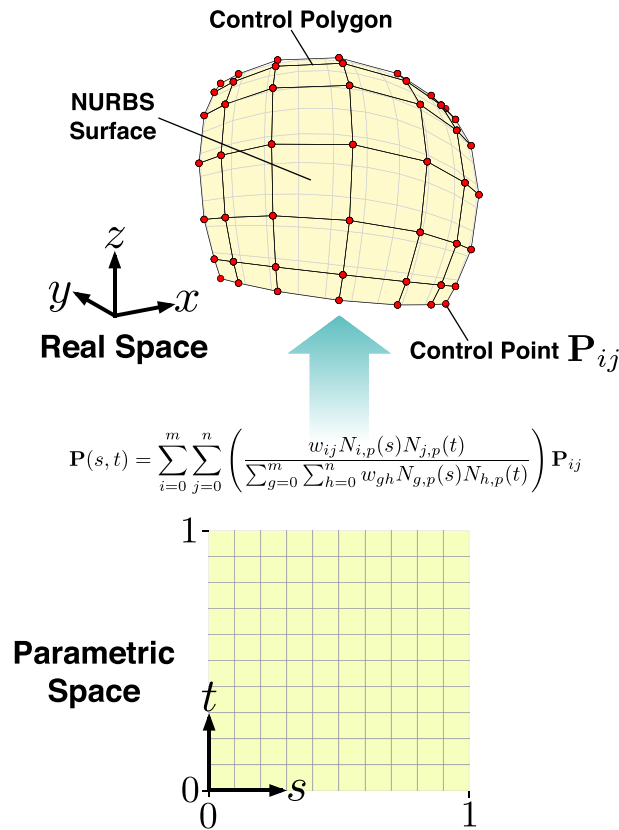


Figure 1. Schematic of a single patch NURBS surface.

With a NURBS surface defined as a tensor product given by Equation (1), the control points must lie topologically in a rectangular grid. This means that a closed surface representation using a single NURBS patch is not possible without generating singularities at two poles where multiple control points collapse to a single point. These singularities can lead to difficulties when performing contact detection in parametric space, and a multipatch approach to representing the grains would then become necessary (see next section).

Finally, geometrical information for grain model construction could be obtained from grain morphologies inferred from X-Ray tomography data [20]. GEM simulations using topologies from X-ray tomography data are already underway and will provide the first calculations of this kind. Geometrical entities, such as, centroid, volume, moment of inertias and product moments for each grain are calculated by using standard NURBS modeling tools such as Rhino [21]. The principal moment of inertias and initial principal body frame orientation are then obtained by solving an eigenvalue problem and fed as input into GEM. This ability to integrate tightly with and quickly access geometrical information from standard NURBS CAD tools highlights GEM's flexibility during model generation.

### 3. CONTACT DETECTION AND FORCE CALCULATIONS

For the sake of clarity and simplicity of presentation, we implement GEM here within the same framework used in classical DEM [16]. This accomplishes two interconnected objectives: it makes extension of DEM codes to GEM much easier and enables GEM to be compatible with DEM codes and procedures. It can be shown that GEM can take a wide range of variations; in particular, it is fully amenable to more complex contact laws such as Hertzian. However, here, a penalty approach is used whereby contact forces between two grains are calculated based on the interpenetration between two NURBS

surfaces. We generalize and implement an intersection-based approach [14, 22, 23] for local contact detection.

Consider two grains that are potentially in contact. To determine the amount of interpenetration between the two grains, we perform the following key steps:

1. For all pairs of patches, with each pair consisting of one patch from each grain, perform surface–surface intersections to determine a closed intersection curve or loop.
2. Approximate the loop centroid and loop normal. The contact normal is taken as the loop normal.
3. With a line in the direction of the loop normal and passing through the loop centroid, perform, for each surface, a curve–surface intersection to determine the contact point.
4. Calculate the overlap as the distance between the two contact points.

It is worth noting that the definition of the contact plane is, in general, not unique. Also, the set of points describing the intersection loop do not, in general, all lie on a common plane. We approximate the loop normal as the cross product of the vectors emanating from the loop centroid to two points on the intersection loop; the two points are selected such that they are separated by an angle of approximately  $90^\circ$  about the loop normal. For smooth surfaces, this approach appears to be a reasonable approximation. A possible refinement would be iterate on the contact plane orientation to maximize the overlap, similar to the common-plane method [6]. In what follows, we expand on the aforementioned steps.

### 3.1. Intersection algorithms

Spline surface–surface (3D) intersection is a non-trivial problem, and the associated algorithms are significantly more complicated and computationally demanding than those in spline curve–curve (2D) intersection used in [1]. We refer the reader to [24] for a review of intersection algorithms for spline or parametric surfaces. For designing the contact procedure in 3D GEM, preliminary numerical experiments suggests that a subdivision approach to detecting the intersection loop provide a reasonable balance between accuracy and robustness, especially across multiple seams in a multipatch representation. The implemented surface–surface intersection algorithm is summarized in Algorithm 1, which is also shown schematically in Figure 2 (see also [19]). In the algorithm, the potentially intersecting NURBS surfaces in real space are subdivided in parametric space by refining the knot vectors in both parametric directions (e.g.,  $s$  and  $t$ ), using the knot insertion procedure described in Section 2 (for more details, the reader is referred to [19]). The subdivision procedure is repeated until a pre-specified tolerance for surface flatness, described in parametric space, is reached.

Once the algorithm has reached the pre-specified flat surfaces, as shown in Figure 2, the surfaces are ‘discretized’ by using triangles to approximate the intersection loop. The discretization to triangles furnishes a simple means to perform surface-to-surface intersection by means of triangle–triangle intersection procedures. For triangle–triangle intersection, we use the procedure described in [25]. The calculated contact point from the curve–surface intersection, however, does lie on the NURBS surface, and one could thereafter extract other parameters such as local curvature, if such information is needed. Upon exit of the intersection algorithm, a convex hull is applied on the set of midpoints of all the collected (disjoint) intersection curves to form a closed polygon approximating the intersection loop, from which the loop centroid is then approximated. To determine the contact point on each surface, we employ a curve–surface intersection algorithm, with the curve passing through the loop centroid and in the direction of the loop normal determined earlier. This problem is usually well-behaved and poses no numerical difficulty. For the algorithmic details of this part, we refer the reader to [19]. Finally, once the intersection loop normal, overlap and contact point on each surface are determined, the normal and tangential forces acting on a grain are calculated as described in the following subsections.

#### Remark 3

A real-space version of Algorithm 1 can also be implemented. The form of the algorithm remains unchanged, and the only required modification is the replacement of the parametric tolerance for surface flatness with a real-space tolerance, for example by using the diagonal length of the real-space bounding boxes of children surfaces. The real-space version would allow for a single NURBS patch with singularities to be used for contact detection (see first example in Section 5).

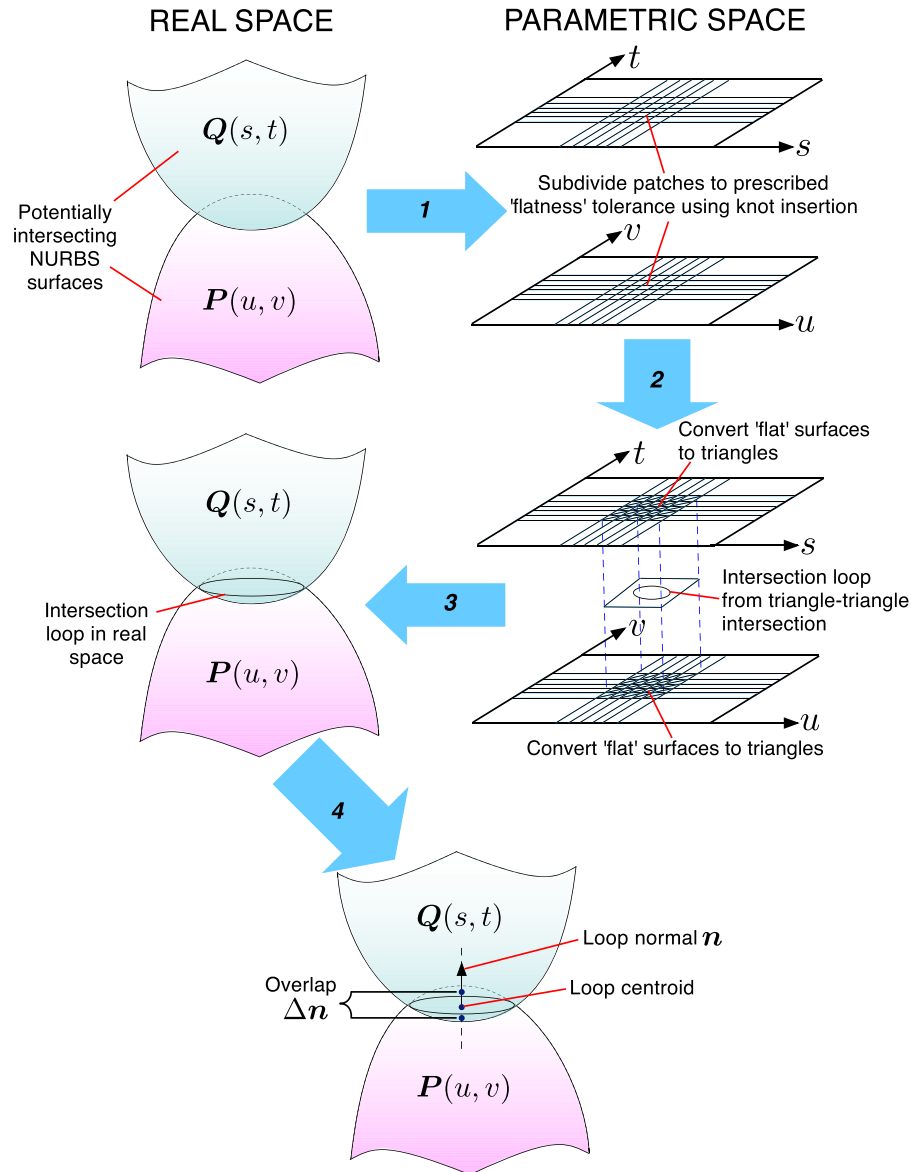


Figure 2. Schematic of steps involved in intersection algorithm.

### 3.2. Normal force and associated moments

Consider a grain  $\Omega^p$  with a contacting neighbor grain  $\Omega^q$  as shown in Figure 3. The effective normal contact force on grain  $\Omega^p$  at the contact point is calculated by using a linear elastic stiffness model such that

$$\mathbf{F}_n^p = -k_n \Delta \mathbf{n} \quad (2)$$

where  $k_n$  is the normal elastic stiffness and  $\Delta \mathbf{n}$  is the overlap, in vector form, determined from the surface-surface intersection problem, compare with Figure 2. The sign convention used is that the normal vector  $\mathbf{n}$  points away from the grain, which means that  $\Delta \mathbf{n}$  has a direction pointing away from grain  $\Omega^p$  and hence the negative sign in Equation (2). By action and reaction, the effective normal contact force on grain  $\Omega^q$  contacting with grain  $\Omega^p$  is then

$$\mathbf{F}_n^q = -\mathbf{F}_n^p. \quad (3)$$



**Algorithm 1** Surface–surface intersection (SSI)**Input:** Two parametric surfaces  $S = \mathbf{P}(u, v)$  and  $T = \mathbf{Q}(s, t)$ **Output:** List of disjoint intersection curves

```

1: procedure SSI( $S, T$ )
2:   if ( bounding boxes of  $S$  and  $T$  do not overlap ) then
3:     return
4:   else if ( parametric domain of surfaces are ‘flat’ enough ) then
5:     Convert surfaces to triangles
6:     Perform triangle-triangle intersection:
7:     if ( triangle-triangle intersection produces a curve ) then
8:       Store intersection curve
9:     end if
10:    return
11:  else
12:    Split  $S$  into 4 children:  $S_1, S_2, S_3, S_4$ 
13:    Split  $T$  into 4 children:  $T_1, T_2, T_3, T_4$ 
14:  end if
15:  Check intersections between  $4 \times 4$  children:
16:  for  $i \leftarrow 1$  to 4 do
17:    for  $j \leftarrow 1$  to 4 do
18:      SSI( $S_i, T_j$ )
19:    end for
20:  end for
21: end procedure

```

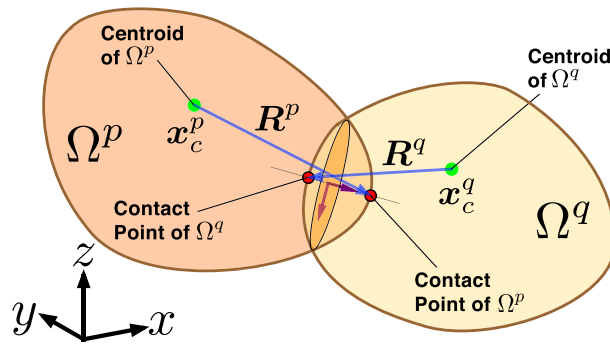


Figure 3. Illustration of two particles ( $\Omega^P$  and  $\Omega^Q$ ) in contact showing interpenetration (overlapping). The moment arms emanating from each particle's centroid to its corresponding contact point are denoted by  $\mathbf{R}^P$  and  $\mathbf{R}^Q$  for  $\Omega^P$  and  $\Omega^Q$ , respectively. Note that overlapping volume is exaggerated for illustrative purposes.

Denoting the moment arm extending from the centroid of grain  $\Omega^P$  to the contact point by  $\mathbf{R}^P$  (as determined in the surface-to-surface intersection problem shown in Figure 2), the moment due to normal force is calculated as

$$\mathbf{M}_n^P = \mathbf{R}^P \times \mathbf{F}_n^P. \quad (4)$$

Similarly, the moment due to normal force on the contacting grain  $\Omega^Q$  is

$$\mathbf{M}_n^Q = \mathbf{R}^Q \times \mathbf{F}_n^Q, \quad (5)$$

where  $\mathbf{R}^Q$  is the moment arm extending from the centroid of grain  $\Omega^Q$  to the contact point.

### 3.3. Tangential force and associated moments

For simplicity, the incremental tangential forces are calculated here by using the simple Coulomb friction model proposed in [16, 26]. In this model, the tangential stiffness is initialized at time of first contact and exists until the grains separate. The velocity of grain  $\Omega^p$  relative to grain  $\Omega^q$  at the contact point is calculated as

$$\mathbf{v} = \mathbf{v}^p + \boldsymbol{\omega}^p \times \mathbf{R}^p - \mathbf{v}^q - \boldsymbol{\omega}^q \times \mathbf{R}^q, \quad (6)$$

where  $\mathbf{v}^p$  and  $\mathbf{v}^q$  are the translational velocities, and  $\boldsymbol{\omega}^p$  and  $\boldsymbol{\omega}^q$  are the angular velocities in global coordinate frame of grains  $\Omega^p$  and  $\Omega^q$ , respectively. We then calculate the incremental displacement as

$$\Delta \mathbf{u} = \mathbf{v} \Delta t. \quad (7)$$

The increment in shear force on grain  $\Omega^p$  is calculated as

$$\Delta \mathbf{F}_s^p = -k_s \Delta \mathbf{s}, \quad (8)$$

where

$$\Delta \mathbf{s} = \Delta \mathbf{u} - (\Delta \mathbf{u} \cdot \mathbf{n}) \mathbf{n} \quad (9)$$

is the tangential incremental displacement obtained by projecting the incremental displacement in the tangential direction. By action and reaction, the increment in shear force on grain  $\Omega^q$  is

$$\Delta \mathbf{F}_s^q = -\Delta \mathbf{F}_s^p. \quad (10)$$

Before the previous shear force can be updated, it needs to be corrected to account for the incremental rotation of the contact plane. The previous shear force vector at the contact point on grain  $\Omega^p$  is first corrected as

$$\mathbf{F}_s^p := \mathbf{Z} \mathbf{F}_s^p, \quad (11)$$

where  $\mathbf{Z}$  is the rotation matrix that rotates the previous normal vector  $\mathbf{n}^{\text{prev}}$  to the current normal vector  $\mathbf{n}$ . The shear force on grain  $\Omega^p$  is updated as

$$\mathbf{F}_s^p := \mathbf{F}_s^p + \Delta \mathbf{F}_s^p \quad (12)$$

and then capped as

$$\mathbf{F}_s^p := \mathbf{F}_s^p \left( \frac{F_{\max}}{\|\mathbf{F}_s^p\|} \right), \quad (13)$$

where

$$F_{\max} = \|\mathbf{F}_n^p\| \tan \phi \quad (14)$$

with  $\phi$  being the interparticle friction angle. Again, by action and reaction, the shear force on grain  $\Omega^q$  contacting with grain  $\Omega^p$  is

$$\mathbf{F}_s^q = -\mathbf{F}_s^p. \quad (15)$$

Finally, the corresponding moments associated with the tangential forces are

$$\mathbf{M}_s^p = \mathbf{R}^p \times \mathbf{F}_s^p \quad (16)$$

$$\mathbf{M}_s^q = \mathbf{R}^q \times \mathbf{F}_s^q \quad (17)$$

for grains  $\Omega^p$  and  $\Omega^q$ , respectively.



*Remark 4*

For simplicity of presentation, the implementation of contact forces and moments discussed earlier correspond to simple linear models. As in standard DEM, the implementation can be extended to nonlinear contact models. We note, however, that the use of local curvature to determine local contact stiffness would require a more careful construction procedure of the multipatch representation to ensure continuity in curvature across seams. In most cases, this is difficult to achieve everywhere (especially using real geometry data inferred from 3D X-ray CT) because enforcing this requirement on a set of connected patches would in general result in changes to the original shape and seam opening on at least one pair of patches. Furthermore, curvature continuity is not possible at junction points where multiple patches meet. Under such conditions, a possible solution would be to relax the seam continuity requirement to at least  $C_0$  continuity and use the average of the curvatures obtained from neighboring patches. Further investigation, however, would be required to justify such an approach.

## 4. DISCRETE EQUATIONS OF MOTION

In the same spirit of enhancing compatibility with DEM as in previous sections, the discrete update equations used here in the context of GEM are identical to those used in classical DEM but we present these developments here for the sake completeness and to show how these update equations are used to update the NURBS surfaces. Here, we assume that the forces and moments, which are induced by contact interactions between grains, are already given (as calculated in the previous sections). We first consider the translational components. The equation governing translational motion of the grain's center of mass is given by Newton's law, as usual,

$$ma_i + C v_i = F_i, \quad (18)$$

where  $i = 1, 2, 3$  in three dimensions,  $m$  is the mass of the grain,  $C = \xi m$  is the damping that proportionally scales the linear velocity  $v_i$ , with  $\xi$  being the global damping parameter. The linear acceleration is given by  $a_i$  and is related to the resultant force  $F_i$ . To integrate the translational components of motion, we employ the centered finite-difference integration scheme proposed in [16].

$$v_i^{n+1/2} = \frac{1}{1 + \xi \Delta t / 2} \left[ (1 - \xi \Delta t / 2) v_i^{n-1/2} + \frac{\Delta t}{m} F_i \right] \quad (19)$$

$$x_i^{n+1} = x_i^n + \Delta t v_i^{n+1/2} \quad (20)$$

The control points of the NURBS patches in the grain are then translated by displacements according to  $\Delta t v_i^{n+1/2}$ .

For the rotational components of motion, it is convenient to work in principal body-fixed frame. For the rest of this section, unless noted otherwise, we work with quantities that are defined with respect to the principal body-fixed frame. Consider the angular accelerations  $\alpha_i$  given through the Euler's equations of motion as

$$\alpha_1 = [M_1 + \omega_2 \omega_3 (I_2 - I_3) - \xi I_1 \omega_1] / I_1 \quad (21)$$

$$\alpha_2 = [M_2 + \omega_3 \omega_1 (I_3 - I_1) - \xi I_2 \omega_2] / I_2 \quad (22)$$

$$\alpha_3 = [M_3 + \omega_1 \omega_2 (I_1 - I_2) - \xi I_3 \omega_3] / I_3, \quad (23)$$

where  $\omega_i$  for  $i = 1, 2, 3$  are the angular velocities,  $M_i$  are the moments and  $I_i$  are the principal moments of inertia. Here, inertia-proportional damping is included via the global damping parameter  $\xi$ . The Euler equations are nonlinear due to the presence of the products of angular velocities on the right-hand side. Therefore, to appropriately integrate the rotational components of motion, we use a predictor-corrector algorithm proposed in [27], which can be described in the following steps:

1. Estimate the angular velocities at the current time step by assuming constant angular acceleration for an additional half step.

$$\omega_i'^n = \omega_i^{n-\frac{1}{2}} + \frac{1}{2} \Delta \omega_i^{n-1}, \quad (24)$$

where  $\Delta \omega_i^{n-1} = \alpha_i^{n-1} \Delta t$ .

2. Calculate angular velocity predictors by using the aforementioned estimates.

$$\Delta \omega_1'^n = \Delta t \left[ M_1^n + \omega_2'^n \omega_3'^n (I_2 - I_3) - \xi I_1 \omega_1'^n \right] / I_1 \quad (25)$$

$$\Delta \omega_2'^n = \Delta t \left[ M_2^n + \omega_3'^n \omega_1'^n (I_3 - I_1) - \xi I_2 \omega_2'^n \right] / I_2 \quad (26)$$

$$\Delta \omega_3'^n = \Delta t \left[ M_3^n + \omega_1'^n \omega_2'^n (I_1 - I_2) - \xi I_3 \omega_3'^n \right] / I_3 \quad (27)$$

3. Predict angular velocities at the current time step.

$$\omega_i^n = \omega_i^{n-\frac{1}{2}} + \frac{1}{2} \Delta \omega_i'^n \quad (28)$$

4. Calculate angular velocity correctors:

$$\Delta \omega_1^n = \Delta t \left[ M_1^n + \omega_2^n \omega_3^n (I_2 - I_3) - \xi I_1 \omega_1^n \right] / I_1 \quad (29)$$

$$\Delta \omega_2^n = \Delta t \left[ M_2^n + \omega_3^n \omega_1^n (I_3 - I_1) - \xi I_2 \omega_2^n \right] / I_2 \quad (30)$$

$$\Delta \omega_3^n = \Delta t \left[ M_3^n + \omega_1^n \omega_2^n (I_1 - I_2) - \xi I_3 \omega_3^n \right] / I_3 \quad (31)$$

Additional iterations are performed by repeating steps 1–4 until the correctors converge to some desired tolerance.

5. Update angular velocities by using the correctors.

$$\omega_i^{n+\frac{1}{2}} = \omega_i^{n-\frac{1}{2}} + \Delta \omega_i^n \quad (32)$$

For small time steps used to resolve the interparticle contacts and for quasi-static conditions in which the angular velocities are small, the number of iterations is typically small. Usually, between three and five iterations are required to achieve machine precision tolerance.

After obtaining the angular velocities, the orientation of the principal body-fixed frame is updated by using the singularity-free quaternion approach in [28], which is described as follows. The rotation matrix that transforms vectors in global space to vectors in body frame is given by

$$\mathbf{A} = \begin{pmatrix} -q_1^2 + q_2^2 - q_3^2 + q_4^2 & -2(q_1 q_2 - q_3 q_4) & 2(q_2 q_3 + q_1 q_4) \\ -2(q_1 q_2 + q_3 q_4) & q_1^2 - q_2^2 - q_3^2 + q_4^2 & -2(q_1 q_3 - q_2 q_4) \\ 2(q_2 q_3 - q_1 q_4) & -2(q_1 q_3 + q_2 q_4) & -q_1^2 - q_2^2 + q_3^2 + q_4^2 \end{pmatrix}, \quad (33)$$

where the  $q_i$ s are the quaternions defined by

$$q_1 = \sin\left(\frac{\theta}{2}\right) \sin\left(\frac{\psi - \phi}{2}\right) \quad (34)$$

$$q_2 = \sin\left(\frac{\theta}{2}\right) \cos\left(\frac{\psi - \phi}{2}\right) \quad (35)$$

$$q_3 = \cos\left(\frac{\theta}{2}\right) \sin\left(\frac{\psi + \phi}{2}\right) \quad (36)$$

$$q_4 = \cos\left(\frac{\theta}{2}\right) \cos\left(\frac{\psi + \phi}{2}\right), \quad (37)$$

and  $\phi$ ,  $\theta$  and  $\psi$  are the Euler angles in the  $z\ x'z'$  notational convention [29]. The initial values of the quaternions are calculated by using the initial configurations of the grains before the start of the simulation.

The time derivatives of the quaternions can be expressed in terms of products of the quaternions with the angular velocities as a singularity-free set of equations

$$\begin{pmatrix} \dot{q}_1 \\ \dot{q}_2 \\ \dot{q}_3 \\ \dot{q}_4 \end{pmatrix} = \frac{1}{2} \begin{pmatrix} -q_3 & -q_4 & q_2 \\ q_4 & -q_3 & -q_1 \\ q_1 & q_2 & q_4 \\ -q_2 & q_1 & -q_3 \end{pmatrix} \begin{pmatrix} \omega_1 \\ \omega_2 \\ \omega_3 \end{pmatrix} \quad (38)$$

with closure of the aforementioned system given by the normalization relation

$$\sum_{i=1}^4 q_i = 1. \quad (39)$$

The aforementioned system of equations can be solved by using an explicit finite difference scheme [27], which results in the following update equation

$$\mathbf{q}^{n+1} = \mathbf{B}^{-1} \mathbf{B}^T \mathbf{q}^n, \quad (40)$$

where

$$\mathbf{q}^n = \begin{pmatrix} q_1^n \\ q_2^n \\ q_3^n \\ q_4^n \end{pmatrix}, \quad \mathbf{B} = \begin{pmatrix} 1 & -\beta_3 & \beta_1 & \beta_2 \\ \beta_3 & 1 & \beta_2 & -\beta_1 \\ -\beta_1 & -\beta_2 & 1 & -\beta_3 \\ -\beta_2 & \beta_1 & \beta_3 & 1 \end{pmatrix} \quad (41)$$

and

$$\beta_i = \frac{\Delta t}{4} \omega_i^{n+\frac{1}{2}} \quad (42)$$

and where  $\square^T$  is the transpose operator. We note that Equation (40) can be solved in closed form as described in [27]. It has been shown in [28] that Equation (38) maintains the orthogonality relation of Equation (39). Normalization of the quaternions, however, is performed after each integration step to prevent normalization failure resulting from round-off error.

The matrix  $\mathbf{A}^{n+1}$  of Equation (33) at  $t_{n+1}$  can be evaluated by using the quaternions in  $\mathbf{q}^{n+1}$ . The updated orientation (triads) of the principal body-fixed frame is then given by the rows  $\mathbf{A}^{n+1}$ . The required rotation matrix for rotating the control points of the NURBS patches about the grain's center of mass is obtained as

$$\mathbf{\Pi}^{n+1} = \mathbf{A}^{n+1T} \mathbf{A}^n. \quad (43)$$

In the next calculation cycle, the moments on each grain due to interparticle contact, calculated in the global frame, are transformed into the principal body-fixed frame by using  $\mathbf{A}^{n+1}$ . The update of the grain through translation and rotation of control points is possible through the affine invariance property of NURBS [18].

## 5. NUMERICAL EXAMPLES

In this section, we present three numerical examples: a verification test, a fully strain controlled test, and a test with mixed boundary conditions. All examples correspond to 3D compression, followed

by macroscopic shear deformations, which induce 3D rotations and displacements at the grain scale. All tests are quasistatic and help demonstrate the ability of GEM to handle complicated grain geometries. Dynamic relaxation is used here to achieve near static equilibrium, by allowing dissipation of accelerations and hence making the sum of all forces vanish [30].

### 5.1. Twenty-seven sphere test

This example serves as a verification test and an assessment of the accuracy of the proposed contact algorithm. An assembly of 27 spheres in simple cubic configuration is prepared within rigid walls, as shown in Figure 4. All spheres are identical, with radius of 50 units and density of 1000 units. This test is the 3D analog of the nine-disk test performed in [1, 16].

We note that the exact sphere representations, each constructed using a single NURBS patch, are required for comparison with results from classical DEM using spheres. As mentioned earlier, the use of a single patch would lead to singularities at two poles, which are problematic in the contact algorithm when the subdivision procedure is performed in parametric space. For purposes of this example, a real-space version of Algorithm 1 is used in which the tolerance is set in real space. This tolerance is set at 0.5 for the first 750 steps to handle tangential or grazing contacts under the initial compression and subsequently set and maintained at 1.0.

The interparticle contact stiffness in the normal direction is  $k_n = 1.35e9$ , and the shear contact stiffness is taken as  $k_s = 2/3k_n$ . Also, the interparticle friction coefficient  $\mu = \tan \phi$ , where  $\phi$  is the interparticle friction angle. The walls are set to be frictionless. In this test, we use two values for the friction angle, that is,  $\phi = 15^\circ$  and  $30^\circ$ , to test the sensitivity of the contact algorithm. The test is carried out with  $\Delta t = 0.01525$  and with sufficient global damping to achieve quasi-static conditions. All six walls are moved inwards with speed  $v_{wall} = 0.12$  for a total duration  $T_{wall} = 2000$  steps. Wall motion is then stopped and the test is allowed to continue for an additional 1000 steps. Subsequently, a constant volume distortion is prescribed by rotating the side walls in the  $x$ -direction at a constant angular velocity of 0.0175 about the  $y$ -direction for 300 steps. The total deformed configuration of the assembly after the first 3000 steps of uniform compression and settlement, and the subsequent 300 steps of constant-volume distortion in the  $xz$  plane is shown in Figure 4.

The average macroscopic stresses are then computed from the interparticle forces as follows. For a macroscopic domain  $\Omega$  with  $N_p$  number of particles, the average macroscopic stresses  $\langle \sigma \rangle$  in a volumetric assembly of granular materials is defined as [31]

$$\langle \sigma \rangle := \frac{1}{\Omega} \int_{\Omega} \sigma \, d\Omega \equiv \frac{1}{\Omega} \sum_{p=1}^{N_p} \Omega_p \bar{\sigma}^p, \quad (44)$$

where

$$\bar{\sigma}^p = \frac{1}{\Omega_p} \sum_{\alpha=1}^{N_c^p} \text{sym}(f^\alpha \otimes x^\alpha) \quad (45)$$

is the average particle stress and  $N_c^p$  is the number of contact forces exerted on particle  $\Omega_p$ . In computing the macroscopic stresses, we use the initial (undeformed) volume of  $300 \times 300 \times 300$ . We compare the accuracy of the proposed contact algorithm with the solutions obtained using classical DEM for the two friction angles considered. The results are shown in Figure 5. We observe that the macroscopic shear stresses from GEM deviate slightly from the classic DEM solutions, but the deviations remain small throughout the test. The macroscopic normal stresses from GEM are in good agreement with the DEM solutions. Given the approximate nature of contact algorithm, we see that the proposed contact algorithm performs very well and robustly.

### 5.2. Strain controlled test: simple (isochoric) shear

A 240-grain assembly is generated by using families of grains with geometries as those shown in Figure 6 and packed in a prismatic container. We construct the grains by using six NURBS patches and enforce at least  $C_0$  continuity across the seams when we stitch the patches. The number of grains of

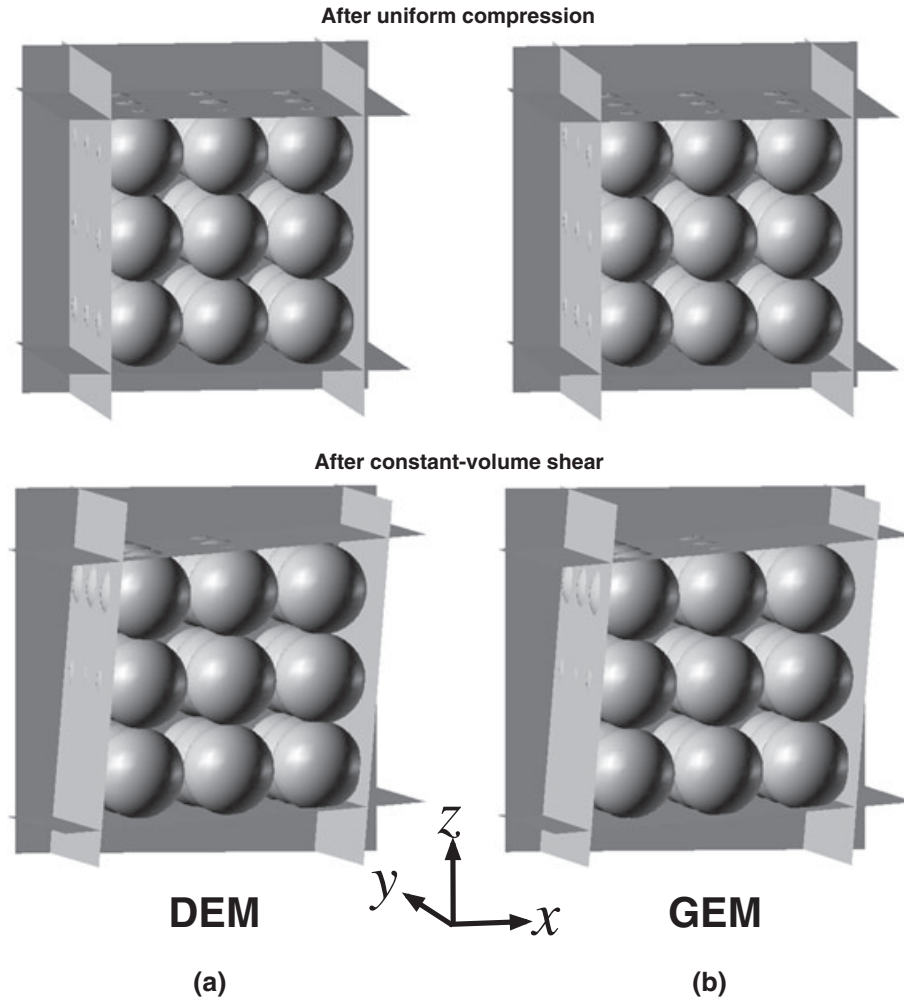


Figure 4. Twenty-seven sphere test. Configurations after uniform compression and constant-volume shear: (a) DEM and (b) GEM.

each shape in the assembly is tabulated in Table I. The initial packing is rendered by randomly placing the 240 grains corresponding to the six shape families shown in Figure 6. The initial packing density is achieved through several stages of wall movements to close the initial gaps between the grains. The container's  $xyz$  dimensions at the end of the packing stage are  $379.75 \times 374.75 \times 421.75$ . The container's walls are also represented as NURBS surfaces. The simulation parameters are specified in Table II.

The loading sequence is defined as follows. First, uniform compression is performed in seven load sequences: each load sequence is comprised of 500 cycles of inward wall movements at a speed  $v_{wall} = 0.125$ , followed by 500 cycles of relaxation, during which wall movements are stopped, and damping is allowed to dissipate energy in the system. The container dimensions at the end of the uniform compression stage are  $371 \times 366 \times 413$ . After a total of 7000 cycles of load/relaxation have been applied, an additional 500 cycles of relaxation are imposed to let the system dissipate some further energy. At the end of this 7500 cycles, a (constant-volume) simple shear deformation in the  $xz$  plane is imposed using 2000 cycles whereby the side walls are rotated about their mid-height at an angular velocity  $\omega_y = 0.005$  clockwise, and the top and bottom walls are moved in the positive and negative  $x$  direction, respectively, at speed  $v_x = \frac{\omega_y h}{2 \cos^2 \theta}$  where  $h = 413$  is the container height, and  $\theta$  is the instantaneous inclination angle of the side walls with respect to the vertical. The aforementioned

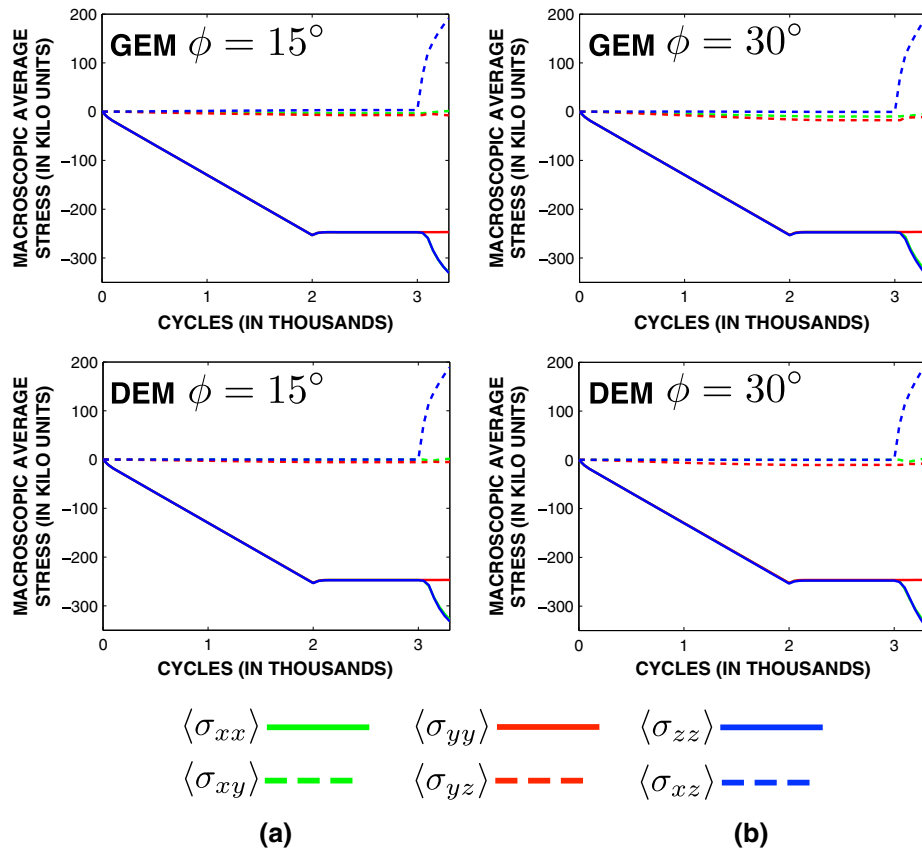


Figure 5. Comparison of macroscopic stresses computed by using GEM and DEM: (a)  $\phi = 15^\circ$  and (b)  $\phi = 30^\circ$ .

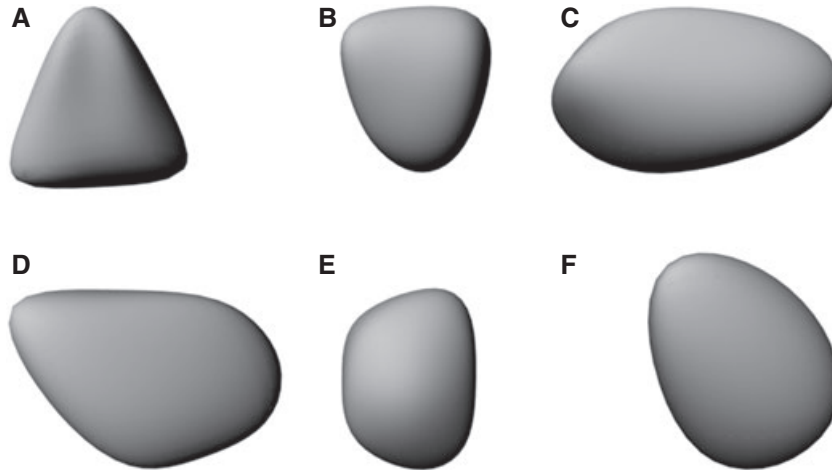


Figure 6. NURBS models showing grain shapes used in this example. Sections with the highest sphericity are shown; all shapes are asymmetrical, that is, no planes of symmetry exist.

wall velocities, global damping coefficient, and apparent density (which also acts as a mass scaling parameter) are chosen to minimize inertia effects (see, e.g., [30] on dynamic relaxation techniques). No contact damping is used here. The configurations after uniform compression and simple shear are shown in Figure 7.

Table I. Number of grains.

Grain shape type	Number
A	24
B	40
C	40
D	40
E	40
F	56
Total	240

Table II. Simulation parameters.

Parameter	Value
Normal contact stiffness $k_n$	$1e8$
Tangential stiffness $k_s$	$\frac{2}{3}k_n$
Interparticle friction angle $\phi$	$25^\circ$
Time step $\Delta t$	0.01
Global damping coefficient $\xi$	1.5 (max)
Density	400

The macroscopic stresses are then calculated by using Equations 44 and 45. For simplicity, we use the macroscopic domain  $\Omega$  volume after initial packing to calculate the macroscopic stresses. The plot of the evolution of the macroscopic stress components are shown in Figure 8. There are several interesting observations that can be made with respect to the evolution of macro and micromechanical states during this test. First, it is apparent that, during the isotropic volumetric compression phase (the first 7500 cycles), the macroscopic stress loses its isotropy. This can be seen after about 4500 cycles, when the normal components of stress start to deviate from each other slightly. This effect is attributed to the potential development of fabric anisotropy in contacts, as evidenced from Figure 9, where it is hard to identify a macroscopically isotropic stress from the observed force chains. The second observation is that during the simple shear deformation phase, the macroscopic shear stress component  $\langle \sigma_{xz} \rangle$  increases, as expected, as a result of the corresponding macroscopic shear deformation imposed. The other macroscopic shear components fluctuate slightly but remain close to zero for the most part. On the other hand, the normal components of the macroscopic stress increase significantly during the simple shear phase as a result of the apparent dilatancy of the sample. As it is known in the granular literature, granular materials dilate (positively or negatively) when deformed in shear. The increase in pressure appears to be a direct result of the dilative tendency of the array when constrained to deform in a macroscopically isochoric manner. The third observation has to do with the alignment of the load chains as depicted in Figure 9. It can be seen that at the end of the isotropic compression phase, the interparticle contact forces are oriented randomly in space, which seems to indicate a relatively isotropic fabric, but as noted earlier, not exactly isotropic. However, after the simple shear phase (after 9500 cycles), the contact forces seem to have an average orientation that is collinear with a line joining the upper left with the lower right edge of the sample. This can be more clearly seen on the 2D projection shown in Figure 9. This shows computationally, for the first time in angular grains, that force chains do align with the directions of macroscopic stresses, as expected from other (spherical) simulations and photoelasticity experiments.

### 5.3. Mixed-strain/stress controlled test

In this example, a shear test with prescribed compression is performed. This test is similar to the one presented before (simple shear), with the added difficulty that the top face of the specimen is prescribed a normal stress (pressure). This essentially enables the sample to freely expand in the direction perpendicular to the top face. Therefore, this test is not isochoric. In the configuration shown in Figure 10,



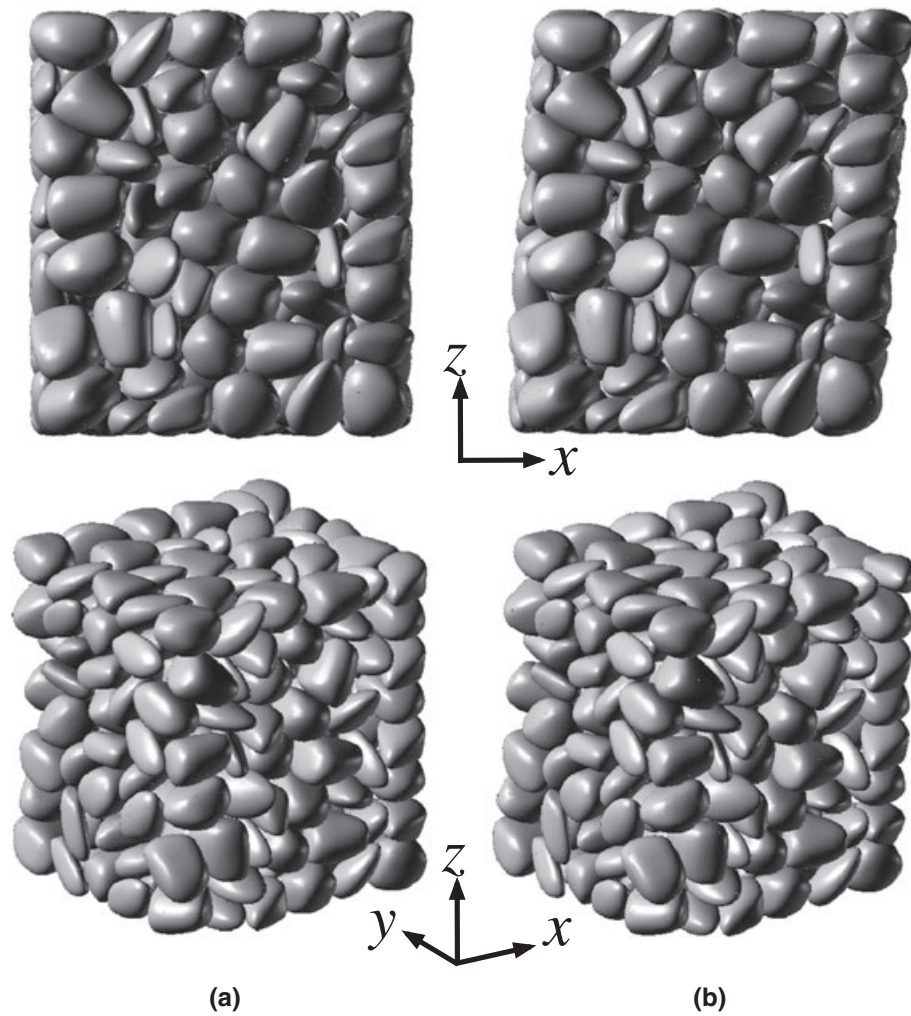


Figure 7. Assembly configuration after (a) uniform compression (cycle 7500) (b) simple shear (cycle 9500).

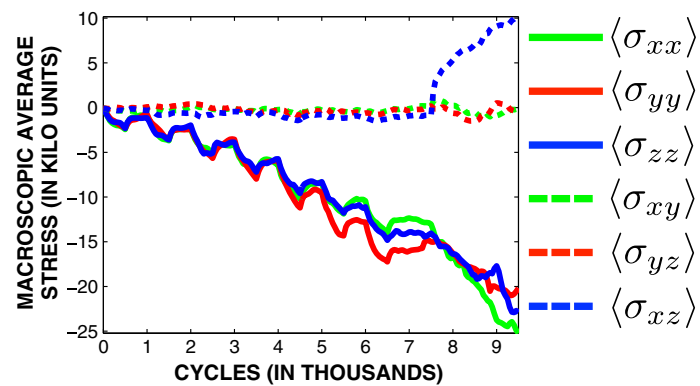


Figure 8. Evolution of the average macroscopic stress components for strain-controlled test.

the component of the stress is prescribed in the  $z$ -direction and, therefore, the displacement of the top face is unspecified in the  $z$ -direction (as opposed to being zero as in the simple shear test). The other boundary conditions are identical to the simple shear test. As for the model parameters, they are the same as before, except of the interparticle friction angle which is  $\phi = 15^\circ$  and the friction

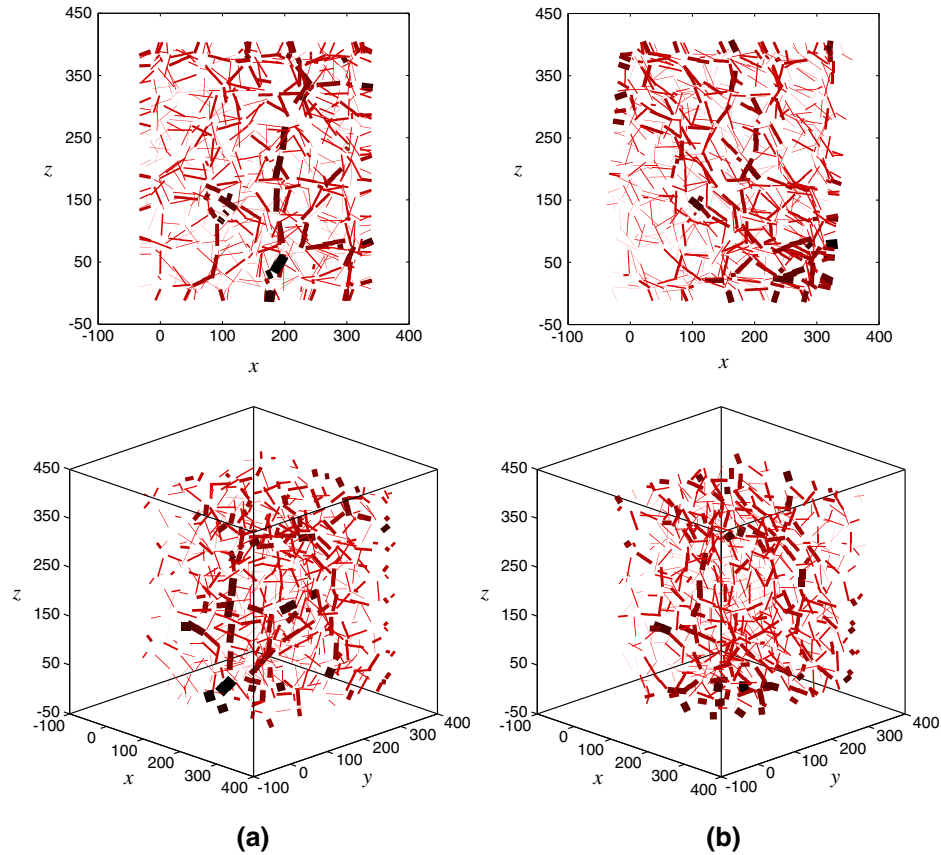


Figure 9. Interparticle force chains after (a) uniform compression (cycle 7500) (b) simple shear (cycle 9500). Darker color and thicker line indicate higher force magnitude.

angle between the walls and particles which is set to zero in this example. These values of friction are picked to study the effect of friction coefficients and the capability of GEM to handle different values of friction.

The granular assembly is initially uniformly compressed by moving the walls inwards at a rate controlled by a feedback loop to achieve an approximate target confinement pressure. Two confinement pressures are considered here: 5 and 10 kilounits. When the target confinement is reached, all wall motions are stopped. Subsequently, a vertical pressure of approximately 5 and 10 kilounits, respectively, is maintained on the top face of the sample to provide a constant confinement during the shear phase. At the same time, the side walls in the  $x$  direction are rotated about  $y$  axis at the base to an angle of approximately 0.15 radians (8.6 degrees); the walls in the  $y$  direction are held fixed, that is, plane strain shear. The deformed configuration of the assembly after the shearing process is shown in Figure 10. The macroscopic deformations in both samples look very similar although some microscopic differences can be noted; in particular, the position of some of the grains is clearly different after shear.

As for the macroscopic results obtained in the tests, the evolution of the average macroscopic stresses during shear for the aforementioned two cases, calculated by using Equation (44), are shown in Figure 11. For each case, the corresponding stress ratio  $q/p$  and volumetric strain  $\epsilon_v$  are plotted against the shear angle  $\gamma$ . From Figure 12, we see that both stress ratios peak when the material is experiencing its most dilative phase, as expected from phenomenology and stress-dilatancy relations [32]. In both cases, the stress ratio and volumetric strain becomes approximately constant at later stages, hence reaching an apparent residual strength, accompanied by a corresponding isochoric state in deformation (critical state). Also, as expected from soil mechanics, we see a relative difference in the behavior as

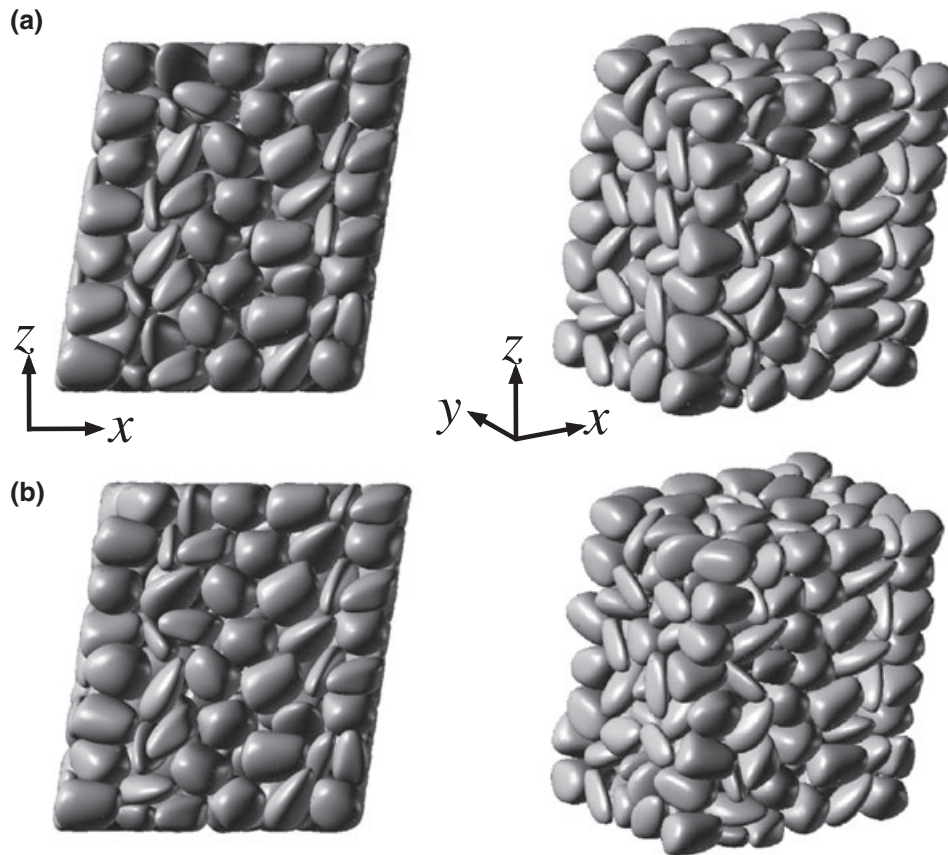


Figure 10. Assembly configurations after shear. Initial confinement of (a) 5 kilounits (b) 10 kilounits.

a function of confining pressure. The sample with less confinement (5 kilounits) exhibits a behavior that is apparently more dilative than that of the more confined sample (10 kilounits). It is expected that the state of the granular material would control the dilative behavior, and in this case, because the void ratio is essentially the same in both cases, the controlling parameter of state is pressure.

Another interesting development is observed in Figure 11, where one can see that, as before, the shear stress  $\langle \sigma_{xz} \rangle$  increases, peaks and then reaches a non-zero residual state. On the other hand, the macroscopic shear stress component  $\langle \sigma_{xy} \rangle$  rises initially, peaks and then decays to zero. This initial increase seems to be associated with an initial rearrangement induced by the macroscopic shear deformation; however, the shear stress  $\langle \sigma_{xy} \rangle$  returns to zero once larger deformations are achieved. The other shear stress  $\langle \sigma_{yz} \rangle$  remains close to zero throughout. Similarly, the normal stresses fluctuate around the initial prescribed amount, with the prescribed normal stress  $\langle \sigma_{zz} \rangle$  faithfully staying very close to the prescribed normal pressure on the top face of the specimen. Although some of these observations and their significance may depend on the specimen size, they do shed light onto the inherent inhomogeneity of the mechanical process taking place at the grain scale, even when the macroscopic process is perfectly homogeneous.

The aforementioned examples illustrate the current capabilities of GEM to capture particle morphology and as a result display some of the salient features of macroscopic behavior observed in granular materials (e.g., sands): stress-dilatancy, state-dependent dilatancy, stress ratio, and residual states. It is expected that the morphology features incorporated in GEM will allow the method to capture material behavior more accurately and therefore be used as a tool to characterize granular materials extensively while connecting the grain and continuum scales. To take the method to that level, some technical developments will need to take place and a thorough validation program will have to be implemented. The next section elucidates some of the technical difficulties and a proposed plan of action.

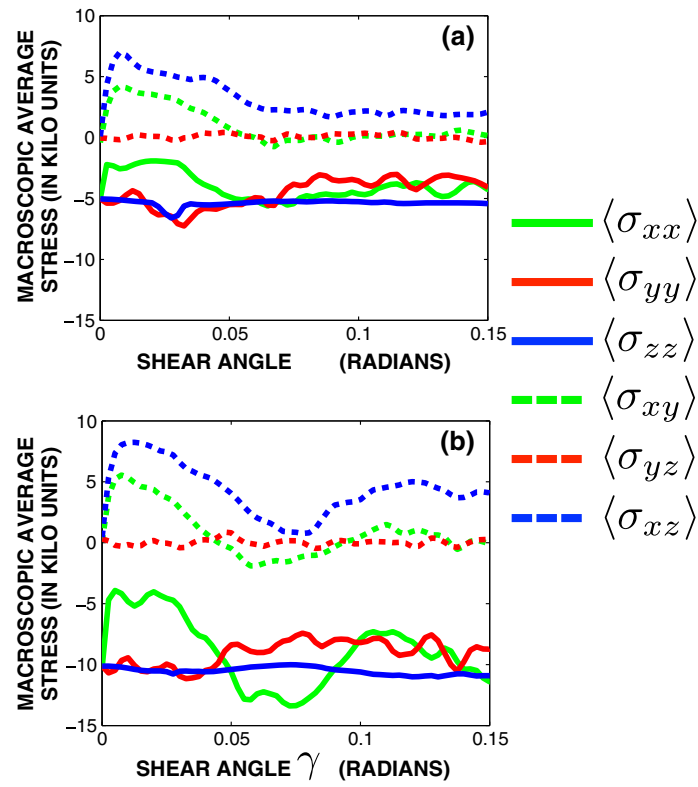


Figure 11. Evolution of the average macroscopic stress components for mixed-boundary tests. Top wall stress of (a) 5 kilounits (b) 10 kilounits.

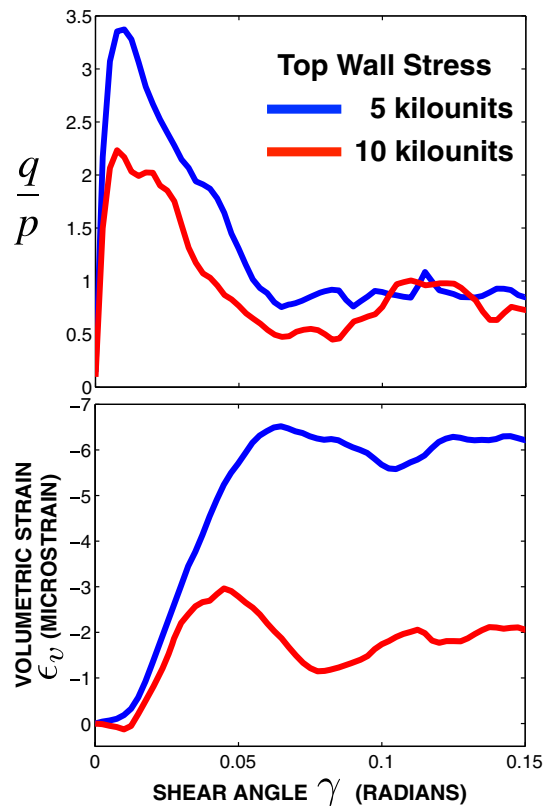


Figure 12. Stress ratio and volumetric strain against shear angle.

## 6. DISCUSSION

In this section, we discuss the computational cost of GEM and outline some of the limitations of our current implementation, as well as identify potential areas of further investigation and improvement. Here, some of the most salient issues are highlighted: computational cost associated with the intersection algorithm, conservation of momentum in dynamic applications, subdivision/intersection procedure, and nonconvexity.

The bulk of the computational cost associated with GEM has to do with the subdivision and intersection approach for determining contact, and it is measurably more expensive than current contact approaches in conventional sphere-based DEM in which the contact overlap can be evaluated analytically and without any iterations. A more appropriate comparison would be to compare GEM with polyhedra-based methods. The tree structure of the subdivision algorithm described in Algorithm 1 is essentially a bounding-volume tree or hierarchy, identical to that used in collision detection algorithms for geometries using polyhedra [33]. As such, the computational cost of GEM is comparable with that of the polyhedra-based methods (to the resolution defined by the subdivision tolerance) with the added cost of memory management associated with the subdivision procedure to create the children surfaces as the tree is traversed. One way to completely eliminate the cost of subdivision is to construct the subdivision tree statically, that is, to keep the subdivision tree constant throughout the simulation, as a one-time pre-processing step before a simulation is performed. With this approach, contact detection is performed by traversing the static tree but performing the intersection calculations using bounding boxes that are mapped from the initial configuration to the current configuration using the total translation vector and total rotation matrix  $\mathbf{A}^{n+1}$  described in Section 4. This approach will endow GEM with the computational cost of polyhedra-based methods. One disadvantage of this approach is the high memory requirement to store the static subdivision tree in-core. A solution between the two extremes of performing the subdivision procedure at each step and constructing a fully static subdivision tree remains to be explored and will require further research. Aside from the foregoing, two additional improvements can be made. First, instead of performing a full-depth traversal of the subdivision tree, an incremental approach similar to that of [34] may be taken. Second, the current intersection algorithm in GEM is serial in nature, and we expect to be able to improve the performance of GEM when algorithms that exploit parallelism (see for e.g., [35]) are utilized.

The difficulties of the spline surface-to-surface intersection problem and limitations of the associated algorithms should also be noted. In GEM, unlike clustering-based or polyhedra-based discrete elements, there are no spheres or vertices/facets to simplify the intersection problem. In addition, because of the nonlinear nature of parametric surfaces, the intersection procedure is iterative. We also note that, in the context of intersection-based contact detection, the difficulty lies primarily in dealing with near tangential intersections. This poses challenges in terms of algorithmic robustness [24]. The subdivision approach used in GEM is convergent in the limit but if used for high-precision results can lead to data proliferation and consequently be computationally inefficient [36]. These issues, however, may be effectively addressed in the future by means of advanced solution procedures and algorithms. The trade off between accuracy, computational cost, robustness, and speed of spline surface-to-surface intersection algorithms in the context of discrete element computations are, at present, not well quantified and should be further investigated.

We have focused our development of GEM for quasistatic applications in which sufficient damping is applied to the system to achieve static equilibrium, and we devised a basic contact procedure to enable the functionality of GEM. For applications in which significant dynamics are involved, the issue of energy and conservation of linear and angular momenta becomes important, as in any DEM-based approach. As such, the effects of the contact procedure on the system's total energy needs to be studied, and the contact procedure may require further improvements. This is true for DEM in general and has received relatively little attention.

With NURBS surfaces, inserting a knot in one parametric dimension causes this new knot to propagate in the other parametric direction, increasing the number of control points. This increase is typically small for simple grain geometries and is therefore not an issue. For complicated grain geometries, however, a large number of control points that carry no significant geometric information could be generated. One possible remedy to this problem is to use T-Splines [37]. T-Splines generalize NURBS



surfaces by allowing a row of control points in a T-mesh (i.e., a T-Spline control polygon) to terminate. This allows the T-mesh to significantly reduce the number of superfluous control points, as well as have local refinement. The T-Spline model is geometrically equivalent to the NURBS model, but with about half as many control points [37]. Therefore, for complicated grain geometries, T-Splines may offer an advantage over NURBS. Intersection algorithms for T-Splines, however, are still a subject of research. The possibility of using T-Splines for discrete element computations will be assessed in the future.

Finally, the extension of GEM to handle nonconvexity will require a convex decomposition methodology. The challenge here is that the decomposition strategy is significantly more complicated than that for polyhedra models. This issue will be investigated in the future. Fortunately, none of these issues are real showstoppers for GEM, and they will tend to disappear once technology improves. Fortunately, NURBS and T-splines are essential to the CAD and graphics industry and hence will most likely experience rapid improvement. Also, the focus of GEM has not yet been efficiency but accuracy. Once the method has demonstrated its accuracy, then the issue of efficiency will be tackled.

## 7. CONCLUSION

We have presented the development of a 3D GEM for computational particle mechanics. GEM provides geometrical enhancements of grain shapes through the flexibility of NURBS. Grain geometrical information can be directly obtained from advanced experiments by using visualization tools such as X-ray CT, already available for natural granular materials such as sands. Leveraging on existing NURBS geometric algorithms, we presented a procedure to perform local contact detection and force calculation, and numerical examples are presented to show this functionality with complex and realistic grain geometries. It was shown that GEM is able to capture some of the most salient features of angular granular matter and that, if proven accurate, it could be used to interrogate material behavior in the future. We highlighted several areas for future work within GEM, with an emphasis on the algorithmic aspects required to make GEM more competitive against the backdrop of conventional DEM. Although GEM is currently more computationally demanding than conventional DEM, GEM provides better accuracy in terms of particle kinematics and contact topology because of improved shape representation capabilities. Extension of GEM to 3D using particle morphologies inferred from 3D X-ray CT data, as well as validation of GEM, are currently underway, and results from these efforts will be reported in the near future. In the development of GEM, we are motivated by the possibility of performing simulations that are comparable in fidelity with X-ray CT-based experiments and that can, for the first time, capture the behavior of natural granular materials such as sands.

## ACKNOWLEDGEMENTS

This work is partially supported by the NSF CAREER Grant No. 1060087 and the AFOSR YIP Grant No. FA9550-11-1-0052 of the California Institute of Technology. This support is gratefully acknowledged.

## REFERENCES

1. Andrade JE, Lim K-W, Avila CF, Vlahinić I. Granular element method for computational particle mechanics. *Computer Methods in Applied Mechanics and Engineering* 2012; **241-244**:262–274.
2. Andrade JE, Tu X. Multiscale framework for behavior prediction in granular media. *Mechanics of Materials* 2009; **41**:652–669.
3. Cho GC, Dodds J, Santamarina JC. Particle shape effects on packing density, stiffness, and strength: natural and crushed sands. *Journal of Geotechnical and Geoenvironmental Engineering* 2006; **132**(5):591–602.
4. Garcia X, Latham J-P, Xiang J, Harrison JP. A clustered overlapping sphere algorithm to represent real particles in discrete element modelling. *Geotechnique* 2009; **59**:779–784.
5. Ashmawy AK, Sukumaran B, Hoang AV. Evaluating the influence of particle shape on liquefaction behavior using discrete element method. In *Proceedings of the Thirteenth International Offshore and Polar Engineering Conference (ISOPE 2003)*: Honolulu, Hawaii, May 2003; 542–549. ISOPE California.
6. Cundall PA. Formulation of a three-dimensional distinct element model. Part I: a scheme to detect and represent contacts in a system composed of many polyhedral blocks. *International Journal of Rock Mechanics and Mining Sciences* 1988; **25**(3):107–116.

7. Hashash YMA, Zhao D, Nezami EG, Ghaboussi J. Three-dimensional discrete element simulation for granular materials. *Engineering Computations* 2006; **23**:749–770.
8. Alonso-Marroquin F, Herrmann HJ. Calculation of the incremental stress–strain relation of a polygonal packing. *Physical Review E* 2002; **66**:021301.
9. Pena AA, Lind PG, Herrmann HJ. Modeling slow deformation of polygonal particles using DEM. *Particology* 2008; **6**(6):506–514.
10. Pournin L, Liebling TM. A generalization of distinct element method to three dimensional particles with complex shapes. In *Proceedings of Powders & Grains*. A. A. Balkema Publishers, Rotterdam: (Balkema, Leiden, 2005), 2005; 1375–1378.
11. Houlsby GT. Potential particles: a method for modelling non-circular particles in DEM. *Computers & Geotechnics* 2009; **36**:953–959.
12. Harkness J. Potential particles for the modelling of interlocking media in three dimensions. *International Journal for Numerical Methods in Engineering* 2009; **80**(12):1573–1594.
13. O'Sullivan C. *Particulate discrete element modelling: a geomechanics perspective*, Applied Geotechnics. Spon Press/Taylor & Francis, 2011.
14. Rothenburg L, Bathurst RJ. Numerical simulation of idealized granular assemblies with plane elliptical particles. *Computers and Geotechnics* 1991; **11**(4):315–329.
15. Ting JM, Khwaja M, Meachum LR, Rowell JD. An ellipse-based discrete element model for granular materials. *International Journal for Numerical and Analytical Methods in Geomechanics* 1993; **17**(9):603–623.
16. Cundall PA, Strack ODL. A discrete numerical model for granular assemblies. *Géotechnique* 1979; **29**:47–65.
17. Hughes TJR, Cottrell JA, Bazilevs Y. Isogeometric analysis: CAD, finite elements, NURBS, exact geometry and mesh refinement. *Computer Methods in Applied Mechanics and Engineering* 2005; **194**:4135–4195.
18. Piegl L, Tiller W. *The NURBS book*, 2nd ed. Springer-Verlag New York, Inc.: New York, NY, USA, 1997.
19. Cohen E, Riesenfeld RF, Elber G. *Geometric modeling with splines: an introduction*. A. K. Peters, Ltd.: Natick, MA, USA, 2001.
20. Vlahinić I, Andrade JE, Andó E, Viggiani G. A method for inferring accurate grain shape and fabric in discrete media using full-fidelity tomographic images. *Granular Matter* (under review).
21. Robert McNeel & Associates. Rhinoceros (Rhino). <http://www.rhino3d.com/>.
22. Hogue C, Newland D. Efficient computer simulation of moving granular particles. *Powder Technology* 1994; **78**(1):51–66.
23. Džiugys A, Peters B. An approach to simulate the motion of spherical and non-spherical fuel particles in combustion chambers. *Granular Matter* 2001; **3**(4):231–266.
24. Skytt V. Challenges in surface-surface intersections. In *Computational Methods for Algebraic Spline Surfaces (COMPASS)*, Dokken T, Jüttler B (eds). Springer-Verlag: Berlin Heidelberg, 2004; 11–26.
25. Möller T. A fast triangle–triangle intersection test. *Journal of Graphics Tools* 1997; **2**:25–30.
26. Hart R, Cundall PA, Lemos J. Formulation of a three-dimensional distinct element model. Part II: mechanical calculations for motion and interaction of a system composed of many polyhedral blocks. *International Journal of Rock Mechanics and Mining Sciences* 1988; **25**(3):117–125.
27. Walton OR, Braun RL. Simulation of rotary drum and repose tests for frictional spheres and rigid sphere clusters. *DOE/NSF Workshop on Flow of Particulates* 1993:1–17.
28. Evans DJ, Murad S. Singularity free algorithm for molecular dynamics simulation of rigid polyatomics. *Molecular Physics* 1977; **34**(2):327–331.
29. Goldstein H, Poole CP, Safko JL. *Classical Mechanics*, 3rd ed. Addison-Wesley: New York, 2001.
30. Tu X, Andrade JE. Criteria for static equilibrium in particulate mechanics computations. *International Journal for Numerical Methods in Engineering* 2008; **75**:1581–1606.
31. Christoffersen J, Mehrabadi MM, Nemat-Nasser S. A micromechanical description of granular material behavior. *Journal of Applied Mechanics* 1981; **48**:339–344.
32. Muir Wood D. *Soil Behaviour and Critical State Soil Mechanics*. Cambridge University Press: Cambridge, UK, 1990.
33. Ericson C. *Real-time Collision Detection (The Morgan Kaufmann Series in Interactive 3D Technology)*. Morgan Kaufmann Publishers Inc.: San Francisco, CA, USA, 2004.
34. Li T-Y, Chen J-S. Incremental 3D collision detection with hierarchical data structures. In *Proceedings of the ACM Symposium on Virtual Reality Software and Technology, VRST '98*. ACM: New York, NY, USA, 1998; 139–144.
35. Krishnamurthy A, Khardekar R, McMains S, Haller K, Elber G. Performing efficient NURBS modeling operations on the GPU. In *Proceedings of the 2008 ACM Symposium on Solid and Physical Modeling, SPM '08*. ACM: New York, NY, USA, 2008; 257–268.
36. Krishnan S, Manocha D. An efficient surface intersection algorithm based on lower-dimensional formulation. *ACM Transactions Graphics* 1997; **16**:74–106.
37. Sederberg TW, Cardon DL, Finnigan GT, North NS, Zheng J, Lyche T. T-spline simplification and local refinement. *ACM Transactions Graphics* 2004; **23**:276–283.